

Key Points:

- Pressure, temperature, and water content dependences of olivine ionic conductivity are obtained
- Olivine ionic conductivity is dramatically enhanced by water incorporation
- Olivine ionic conductivity may contribute significantly to the bulk conductivity of olivine in the asthenosphere

Supporting Information:

- Supporting Information S1

Correspondence to:

H. Fei,
hongzhan.fe@uni-bayreuth.de

Citation:

Fei, H., Druzhbin, D., & Katsura, T. (2020). The effect of water on ionic conductivity in olivine. *Journal of Geophysical Research: Solid Earth*, 125, e2019JB019313. <https://doi.org/10.1029/2019JB019313>

Received 26 DEC 2019

Accepted 2 MAR 2020

Accepted article online 5 MAR 2020

Abstract High-temperature ionic conductivity in olivine single crystals has been measured in the [100], [010], and [001] crystallographic orientations as a function of pressure from 2 to 10 GPa, temperature from 1450 to 2180 K, and H₂O content from 20 to 580 wt. ppm using multianvil presses with in situ impedance analyses. The experimental results yield an activation energy, activation volume, and H₂O content exponent of 250–405 kJ/mol, 3.2–5.3 cm³/mol, and 1.3 ± 0.2, respectively, for the high-temperature ionic conduction regime. Olivine ionic conductivity has negative pressure and positive temperature dependences and is significantly enhanced by H₂O incorporation. The [001] direction is more conductive than the [100] and [010] directions. The H₂O-enhanced ionic conductivity may contribute significantly to the electrical conductivity profile in the asthenosphere, especially in the regions under relatively high-temperature and low-pressure conditions.

1. Introduction

Olivine is the dominant mineral in the Earth's upper mantle. It has been proposed that olivine has three electrical conduction mechanisms (e.g., Yoshino et al., 2009): (a) proton conduction with charges carried by protons (H_i[•]) produced by (2H)_{Mg}^x ⇌ H_{Mg}' + H_i[•] owing to the small amount of H₂O (protons) incorporated in the crystal structure as point defects; (b) small polaron conduction caused by hopping of electron holes (h[•]) between ferrous and ferric iron, that is, Fe³⁺ ⇌ Fe²⁺ + h[•], with h[•] as the charge carrier; and (c) ionic conduction controlled by the diffusion of ions between regular sites and vacancies, A_A^x (site 1) + V_A (site 2) ⇌ V_A (site 1) + A_A^x (site 2), where A_A^x is the regular site of element A (Mg, Fe, Si, and O) and V_A is the corresponding vacant site. Mechanism (c) is dominated by Mg (Fe) diffusion because it is by orders of magnitude faster than Si and O in olivine (Chakraborty et al., 1994; Fei et al., 2013, 2014; Fei et al., 2018a). The charge carrier of ionic conduction is specialized to vacancies on regular sites (also called vacancy conduction; e.g., Gardés et al., 2014), although protons in olivine are also ionic species. The proton, small polaron, and ionic conduction mechanisms dominate olivine conductivity at relatively low (<~1200 K), moderate (~1200–1750 K), and high (>~1750 K) temperatures, respectively, owing to their different temperature dependences (Constable et al., 1992; Constable, 2006; Gardés et al., 2014; Yoshino et al., 2009).

To understand the electrical conductivity profiles in the upper mantle, a series of experimental studies have been performed to measure the proton and small polaron conductivities in olivine (e.g., Du Frane et al., 2005; Dai & Karato, 2014a, 2014b; Poe et al., 2010; Wang et al., 2006; Xu et al., 1998; Yang, 2012). Their results suggest that the proton conduction is significantly enhanced by water incorporation. It may account for the magnetotellurically detected anomalously high and highly anisotropic electrical conductivity (10⁻¹–10⁻² S/m) in the asthenosphere at 70–120 km depth beneath young plates near the East Pacific Rise (Baba et al., 2006; Evans et al., 2005), which cannot be explained by small polaron conductivity in dry olivine. However, this idea was later refuted (e.g., Gardés et al., 2014, 2015; Yoshino et al., 2006, 2009) because newer experimental results show that proton conductivity even in H₂O-saturated olivine is insufficient to explain the highly conductive asthenosphere.

The ionic conduction mechanism, in contrast, has received only minimal attention because its contribution to olivine bulk conductivity is considered to be significant only at temperatures above 1750 K (e.g., Constable et al., 1992), which is unrealistically high for the majority of asthenosphere. However, this conclusion is based on dry olivine experiments. Incorporation of H₂O produces additional point defects on Mg (Fe) sites (Demouchy & Mackwell, 2006; Kohlstedt & Mackwell, 1998) and enhances the exchange of Mg (Fe) ions between regular and vacant sites (Fei et al., 2018a, 2018b), which is expected to raise the ionic conductivity. Therefore, although the contribution of ionic conductivity is negligible in dry olivine at asthenospheric temperatures (<1750 K), it may become significant by considering small amounts of H₂O in the asthenosphere

© 2020. The Authors.

This is an open access article under the terms of the Creative Commons Attribution License, which permits use, distribution and reproduction in any medium, provided the original work is properly cited.

(Fei et al., 2018a). To evaluate this hypothesis, knowledge about the H₂O-content dependence of olivine ionic conductivity is required. However, such experimental results have not been reported because olivine dehydration occurs at high temperatures (Yoshino et al., 2009), and the temperature range of previous H₂O-effect related studies was therefore limited to ~1400 K (e.g., Dai & Karato, 2014a; Wang et al., 2006; Yang, 2012), which is insufficient for observing ionic conduction.

In this study, we measured the conductivity of olivine single crystals at pressures of 2 to 10 GPa, temperatures of 1400 to 2180 K, and H₂O contents of ~20 to 580 wt. ppm along the [100], [010], and [001] crystallographic axes. Our results demonstrate that olivine ionic conductivity is enhanced by H₂O incorporation and may contribute significantly to the bulk conductivity of olivine under asthenospheric conditions.

2. Experimental and Analytical Methods

2.1. Starting Material

Three pieces of handpicked natural olivine single crystals from Pakistan with grain sizes of ~15 mm were used as the starting material. The initial H₂O content of the crystals was about 50 wt. ppm from infrared analysis, and the Fe/(Mg + Fe) atomic ratios were 9.0–9.5% by electron microprobe measurements. Trace element contents were reported in Gose et al. (2010). After orientation to the [100], [010], and [001] crystallographic directions using a single-crystal X-ray diffractometer, inclusion-free disks with a 1.0-mm diameter and 0.3-mm thickness were cored from the single crystals along crystallographic directions and used for the following conductivity measurements.

2.2. Multianvil Cell Assembly

Each olivine disk was sandwiched by two Mo electrodes, each of which consisted of one or two layers of Mo disks with a 1.0-mm diameter and 0.025 mm thickness. The sample was insulated by an MgO single-crystal sleeve and shielded by a Mo foil, which prevented the migration of conductive materials from the graphite furnace into the MgO insulator at high temperature. In Runs H4721 and H4745 (Table 1), small amounts of brucite powder were placed between the two Mo disks of each electrode as a H₂O source. The volume ratio of brucite to olivine is about 1/50, corresponding to ~6,000 wt. ppm bulk H₂O in olivine + brucite. A ZrO₂ sleeve surrounding the furnace was used as a thermal insulator. An MgO (+5 wt.% Cr₂O₃) octahedron with 18 mm edge lengths acted as a pressure medium. A pair of W₉₇Re₃-W₇₅Re₂₅ wires (D-type thermocouple) was connected to one electrode to measure the sample temperature, and another W₉₇Re₃ wire was connected to the other electrode for impedance analyses (Figure 1).

2.3. High *P-T* Experiments

After assembly, each cell was dried in a vacuum oven at 420 K for 24 hr, then loaded into a multianvil press and compressed to 2 or 4 GPa at room temperature using eight tungsten carbide cubes with edge lengths of 32 mm and truncated edge lengths of 11 mm. From test experiments, it was found that even with drying in the vacuum oven, some moisture remains in the pressure medium. The assembly was therefore heated to 1300 or 1500 K and maintained for a few hours until no decrease in apparent sample conductivity with time was observed. The pressure was then increased to the desired values of 2 to 10 GPa, and two to five heating-cooling cycles up to 2180 K were performed with a step of 30–100 K in each pressure stage. In each step, the sample was heated/cooled to the target temperature at a rate of ~100 K/min, followed by impedance analysis, which took 1–3 min. The duration of each heating-cooling cycle was 1–2 hr depending upon the temperature range. The assembly was quenched to room temperature by switching off the heating power and decompressed to ambient pressure over 10 hr.

As mentioned in section 1, olivine dehydration has prevented the investigation of H₂O dependence of conductivity at very high temperatures (Yoshino et al., 2009). Dehydration was also observed in this study: H₂O content ($C_{\text{H}_2\text{O}}$) decreases from 50 to 20 wt. ppm after heating above 1700 K. Therefore, although the low- $C_{\text{H}_2\text{O}}$ runs (~20 wt. ppm) (I471, I511, and H4674) were performed up to 2200 K; the temperature was limited to 1700 K for higher- $C_{\text{H}_2\text{O}}$ runs (H4694, H4721, and H4745) (Table 1). To clearly observe ionic conductivity at relatively low temperatures, measurements were performed in the [010] and [001] directions, along which small polaron conductivity and ionic conductivity are the lowest and highest, respectively (Constable et al., 1992).

Table 1
Run Summary and Fitting Parameters From Equation 2

| Axis | Run No. | Pressure (GPa) | Temperature (K) | Duration (hr) | C_{H_2O} (wt. ppm) | /abs | Fe/(Mg + Fe) (%) | $\text{Log}\sigma_{\text{ionic},0}$ (K·S/m) | E_{ionic} (kJ/mol) | V_{ionic} (cm^3/mol) | $\text{Log}\sigma_{\text{sp},0}$ (S/m) | E_{sp} (kJ/mol) | V_{sp} (cm^3/mol) |
|-------|--------------------|----------------|-----------------|---------------|----------------------|------------|-------------------|---|-----------------------------|---|--|--------------------------|--|
| [100] | 1471 | 2, 4, 6, 8 | 1480–2080 | 11.5 | 20 (8) | 1.01/0.033 | 6.6 (4) | 11.6 (1) | 337 (15) | 4.2 (4) | 1.5 (2) | 117 (13) | 0.5 (7) |
| [010] | 1511 | 2, 4, 6, 8 | 1400–2180 | 14.0 | 18 (9) | 1.01/0.018 | N.D. ^b | 13.2 (3) | 396 (25) | 3.2 (2) | 2.7 (2) | 163 (25) | −0.2 (2) |
| [010] | H4745 ^a | 2, 4 | 1400–1650 | 6.0 | 580 (40) | 1.25/0.509 | 7.7(8) | 15.8 (1) | 406 (3) | 4.9 (5) | 1.7 (4) | 114 (8) ^d | −0.9 (13) |
| [001] | H4674 | 2, 4 | 1500–1970 | 6.5 | 21 (9) | 1.00/0.014 | 8.7(10) | 13.5 (3) | 385 (15) | 4.1 (4) | 2.7 (3) | 139 (13) | 0.5 (7) |
| [001] | H4721 ^a | 4, 6, 8, 10 | 1400–1660 | 6.4 | 270 (30) | 1.10/0.204 | 8.6(15) | 10.8 (7) | 247 (20) | 5.3 (6) | 1.2 (1) | 86 (33) ^d | 0.0 (8) |
| [001] | H4694 | 4 | 1540–1700 | 2.0 | 37 (8) | 1.01/0.029 | N.D. ^b | 11.4 (1) | 305 (9) ^c | N.D. ^b | 1.4 (1) | 100 (8) ^{c,d} | N.D. ^b |

Note. Error bars represent one standard deviation in data statistics/fitting without the uncertainty of individual data points. The initial C_{H_2O} are about 50 wt. ppm for all the runs. The is the correction factor in equation 1, and abs is the maximum infrared absorbance at $3,000\text{--}4,000\text{ cm}^{-1}$. The data of fitting are given in the general repository, Zenodo (doi: 10.5281/zenodo.3386773). ^a(Brucite was used as water source in H4745 and H4721). ^bN.D.: Not determined. ^cThe E_{ionic} and E_{sp} of Run H4694 are calculated from $E = H - PV$, where H is the activation enthalpy obtained at 4 GPa, and V is determined in H4674 and H4721. ^dOwing to the H_2O -rich conditions in H4745, H4721, and H4694, the activation energy of the low-temperature conduction regime is substantially lower than in other runs; therefore, the small polaron conduction is probably masked by other mechanisms (e.g., proton conduction) as explained in the main text.

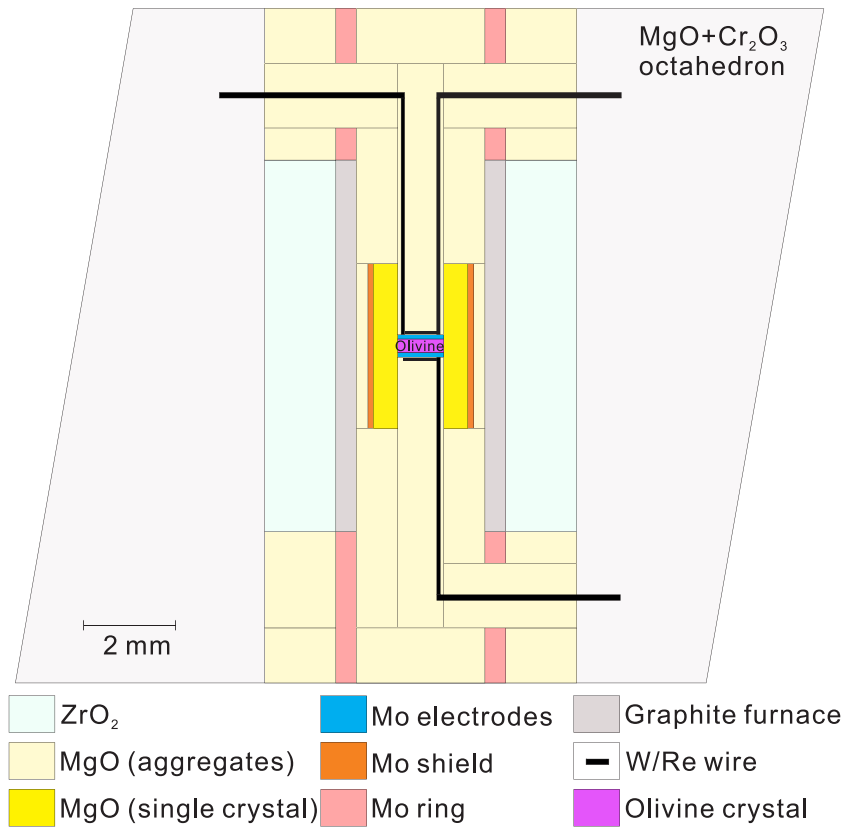


Figure 1. Cross section of a multianvil cell assembly used for the conductivity measurements.

2.4. In Situ Impedance Analysis

In situ impedance analysis was performed using a Solartron 1260 Impedance/Gain Phase analyzer. In each measurement, an alternating voltage (1 V) with a frequency swept from 10^7 to 10^2 –1 Hz with 20 steps per decade was applied to the electrodes, and the complex impedance was recorded at each frequency (Figure 2). The sample resistance R was obtained by fitting the impedance spectrum to an equivalent parallel circuit with a resistor and constant phase element using the impedance analysis software, Z-View.

Conductivity (σ) under given pressure and temperature conditions was calculated from the formula $\sigma = 4L/(\pi d^2 R)$, where L and d are the thickness (0.3 mm) and cross-sectional diameter (1.0 mm) of the sample, respectively (Fei et al., 2017).

The L and d had no distinct change (less than 5% shortening) before and after the high-pressure experiments. The background conductivity of the cell assembly was examined by Fe-free forsterite samples, whose conductivity is more than 1 order of magnitude lower than those in the olivine samples. The fitting of impedance spectrum causes negligible error on σ (<1%). Additionally, the variation of Fe% (from 6.6% to 8.7% in Table 1) may affect the ionic conductivity in dry olivine by a maximum of ~30% in dry olivine (section 3.2). Therefore, the total uncertainty of σ is by a maximum of 50%. This maximum uncertainty is also confirmed by the variation of data points in different heating-cooling cycles (Figure 3).

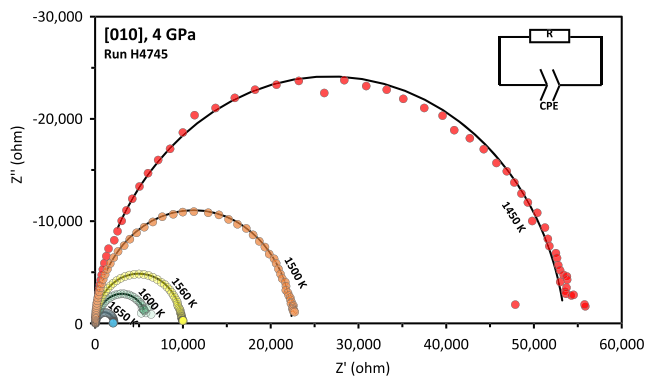


Figure 2. Example of complex impedance spectra (Run H4745) where Z' and Z'' are the real and imaginary parts, respectively. The frequency sweeps from 10^7 (left) to 10^2 –1 Hz (right). The solid lines are fitting curves by Z-view software with a resistor and constant phase element parallel circuit.

2.5. Infrared Analyses

The recovered cell assemblies were double-side polished and Fourier transform infrared (FTIR) spectroscopy analysis was performed along

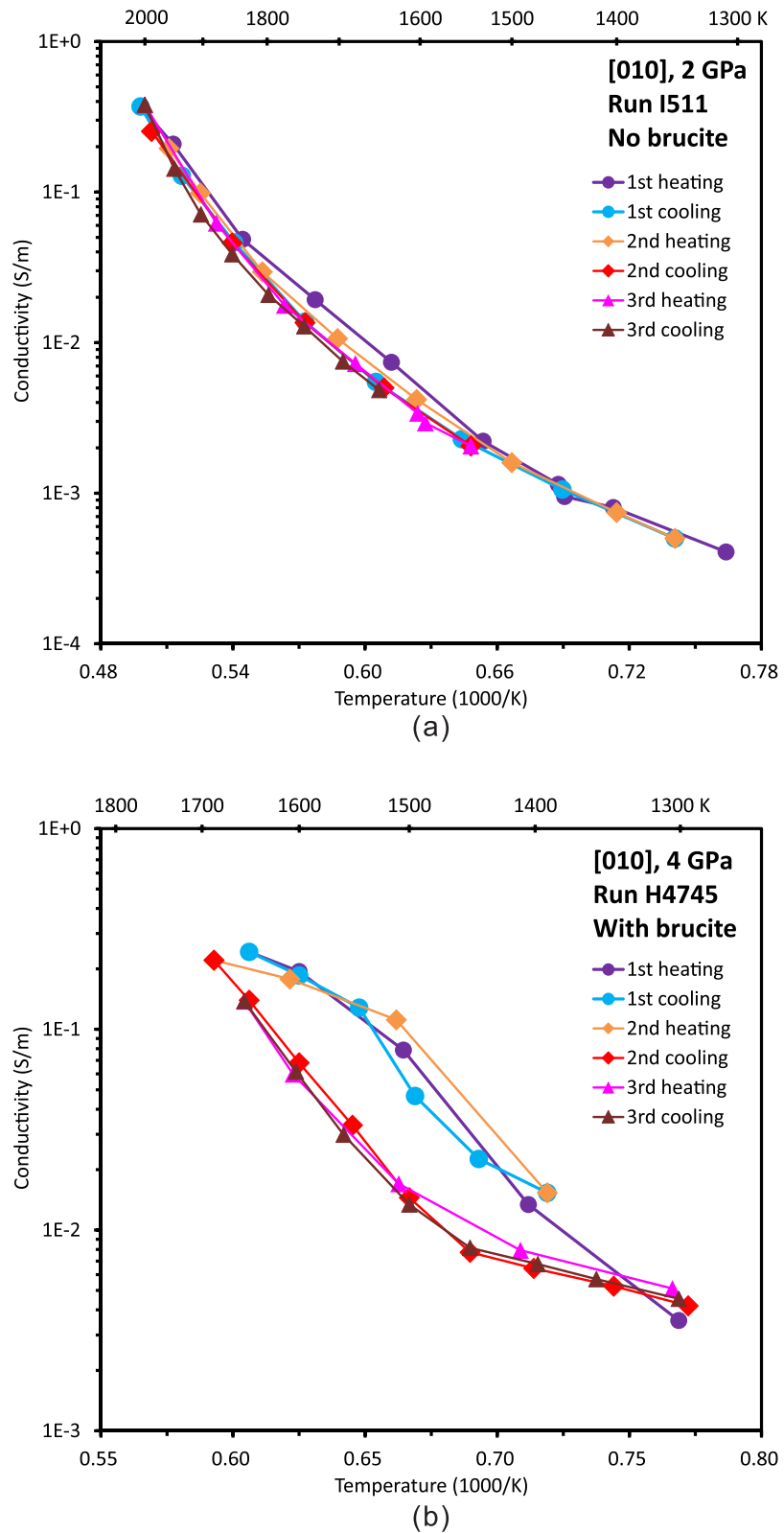


Figure 3. Example of conductivity values obtained in heating-cooling cycles. (a) Brucite-free (I511). (b) Brucite-bearing (H4745). The conductivity obtained in the first or second cooling and further heating-cooling cycles are repeatable. Only the first (or second) heating paths have slightly higher values. The repeatable data points in different heating-cooling cycles also indicate a maximum uncertainty of <50% for σ determination.

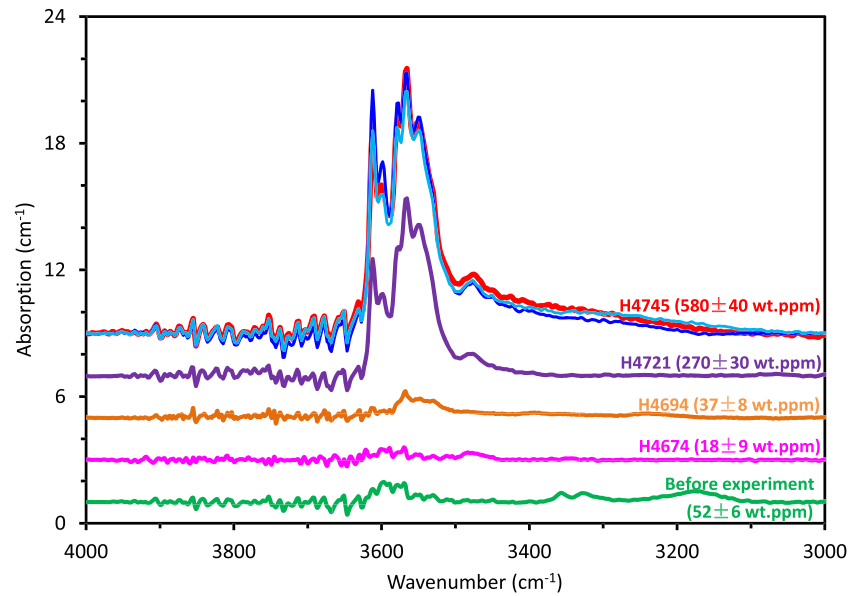


Figure 4. Example of infrared spectra after baseline subtraction and thickness normalization to 1 cm. The spectra are vertically shifted for visibility. Different areas of the sample show identical FTIR spectra (Run H4745, red: 620 wt. ppm, blue: 579 wt. ppm, and cyan: 539 wt. ppm), indicating homogenous H₂O distribution in the sample.

the cross sections using an unpolarized beam with a 30–60 μm diameter. Three or four infrared spectra in different regions (center and near the edge) of each sample were obtained. No essential differences in spectra were observed among the different regions, indicating homogeneous H₂O distribution (Figure 4). The H₂O contents were calculated by integration of the infrared absorptions from 3,000 to 4,000 cm⁻¹,

$$C_{\text{H}_2\text{O}} = 3 \times \zeta \times 0.119 \times \int_{3000}^{4000} A(\nu) d\nu \quad (1)$$

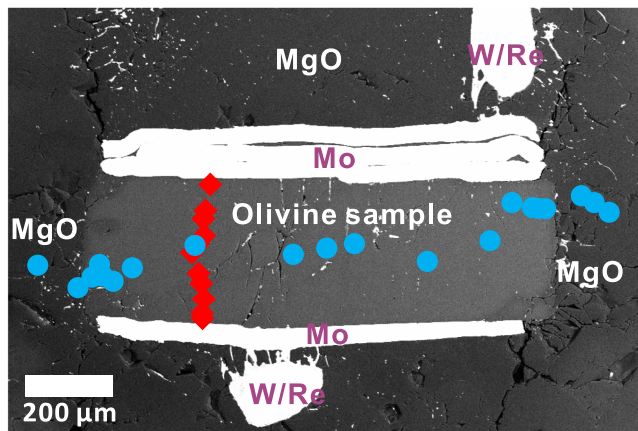
where $C_{\text{H}_2\text{O}}$ is the H₂O content in wt. ppm, 0.119 is the calibration based on polarized FTIR from Withers et al. (2012), ζ is the correction factor for unpolarized light ($\zeta \approx 1$ to 1.25 listed in Table 1 upon maximum absorbance (Withers, 2013)), and $A(\nu)$ is the absorption coefficient at wavenumber ν after background subtraction and thickness normalization to 1 cm.

Polarized FTIR on oriented crystals may give more precise $C_{\text{H}_2\text{O}}$. In that case, however, the crystals should be polished along three crystallographic orientations, which is unfavorable here because the orientation and polishing process would damage the cross section of the assembly and prohibit any further observations. Therefore, only unpolarized FTIR spectra were measured on a single plane for each sample, which may introduce uncertainties in $C_{\text{H}_2\text{O}}$ evaluation (see section 3.3). Additionally, different infrared calibrations yield different $C_{\text{H}_2\text{O}}$. If using the Bell et al. (2003) calibration, the absolute values of $C_{\text{H}_2\text{O}}$ are higher by about 50%, although the $C_{\text{H}_2\text{O}}$ -exponent for ionic conductivity reported in this study should remain the same.

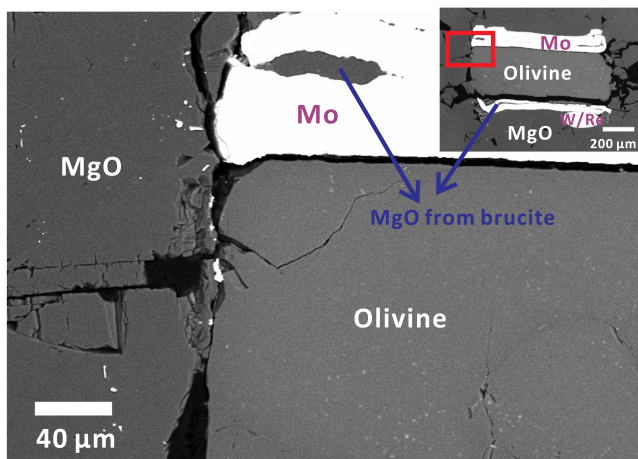
3. Results and Discussion

3.1. Dehydration or H₂O-Reabsorption During Conductivity Measurements

To investigate the $C_{\text{H}_2\text{O}}$ dependence of olivine conductivity, it is necessary to know $C_{\text{H}_2\text{O}}$ in the samples during conductivity measurements. However, $C_{\text{H}_2\text{O}}$ is only measured by FTIR in the recovered samples after conductivity measurements. Because the actual $C_{\text{H}_2\text{O}}$ during each impedance spectrum acquisition is unknown, we evaluate the dehydration during heating paths and H₂O-reabsorption during cooling paths according to the conductivity variation. It is expected that if significant dehydration had occurred continuously, the conductivity should have continuously decreased upon repeating heating-cooling cycles because the ionic conductivity is $C_{\text{H}_2\text{O}}$ -dependent as shown later. Nevertheless, Figure 3 shows that, although the conductivity decreases in the first (and second) heating-cooling paths, changes were negligible in the later



(a)



(b)

Figure 5. Backscattered SEM images of the recovered samples. (a) Brucite-free (I471). The thermocouple wires were initially in contact with Mo but partially polished away during cross-section preparation. The red and blue spots are electron microprobe analysis positions in Figures 6a and 6b, respectively. (b) Brucite-bearing (H4721). No melt phase is observed even in the regions near the MgO-olivine-Mo junction, which is the most likely region to form melt (brucite was initially between the Mo foils). The bright particles are metal from the thermocouple likely caused by polishing.

paths. We therefore expect that olivine dehydration has occurred mostly in the first (and second) heating paths, but is insignificant in later heating-cooling paths. On the other hand, H₂O reabsorption is also unlikely to occur; otherwise, conductivity should have increased, rather than obtaining repeatable values in different heating-cooling cycles.

The above evaluation of C_{H_2O} variation relies on the extent of C_{H_2O} that can produce measurable changes in conductivity. This is unknown because both conductivity and C_{H_2O} are variables, and therefore insignificant dehydration during heating and H₂O-reabsorption during cooling is still theoretically possible (Karato, 2019). In that case, the C_{H_2O} under higher-temperature conditions for the ionic conduction regime would be slightly underestimated; namely, the conductivity is enhanced by less H₂O, which further supports our conclusion.

3.2. Microstructure and Composition of the Recovered Samples

Scanning electron microscopy (SEM) observations of recovered assemblies show that olivine and electrodes remain in a sandwiched structure (Figures 5a and 5b). Cracks are found within olivine crystals, which should be caused mechanically by compression and/or decompression. Nevertheless, even with cracks, the measured conductivity data still represent that for single crystal rather than polycrystalline because there is no recrystallization process, therefore, the crystallographic orientation should remain. This is confirmed by the experimental results which shows strong conductivity anisotropy. As expected, no melts or fluid phases are observed near the samples or within cracks for both brucite-bearing and brucite-free runs.

Electron microprobe analysis show lower Fe contents in the recovered samples (Table 1). The Fe/(Mg + Fe) ratio does not show any systematic variation along the axial cross section but clearly decreases near MgO along the radial cross section (Figures 6a and 6b). The decrease of bulk Fe content in olivine is therefore owing to Mg-Fe exchange between olivine and MgO, rather than absorption by Mo. Because the samples are radially surrounded by MgO, the vacancy concentration on Mg (Fe) site should remain constant by Mg-Fe exchange despite a slight decrease in the Fe/(Mg + Fe) ratio, and ionic conductivity should therefore be unaffected. In view of defect chemistry, the defect concentration on the Mg (Fe) site is related to Fe³⁺ in dry olivine with a charge balance of $[Fe^{3+}] = 2[V_{Mg}^{''}]$ (Kohlstedt, 2006; Stocker & Smyth, 1978). Under a given oxygen fugacity condition, the $[Fe^{3+}]/\Sigma Fe$ ratio should be fixed (Stocker & Smyth, 1978); thus, we have $[V_{Mg}^{''}] \propto \Sigma Fe$. The variation of Fe% (Table 1)

will have very limited effect on the ionic conductivity in dry olivine. For hydrous olivine, the $[V_{Mg}^{''}]$ is controlled by H₂O content and independent of ΣFe (Kohlstedt, 2006; Kohlstedt & Mackwell, 1998).

3.3. P , T , C_{H_2O} , and Crystallographic Orientation Dependences of Ionic Conductivity

An example of the conductivity (σ) and temperature (T) relationship is shown in Figure 7. The slope of the σ - $1/T$ curve increases with increasing temperature owing to the change of the dominant conduction mechanisms. The contribution of the proton conduction mechanism is difficult to quantify, as discussed in the supporting information. Because this study focuses on the ionic conductivity at asthenospheric temperatures, only data points at temperatures higher than 1400 K are plotted in Figure 8 and fitted to the Arrhenius equation with two terms,

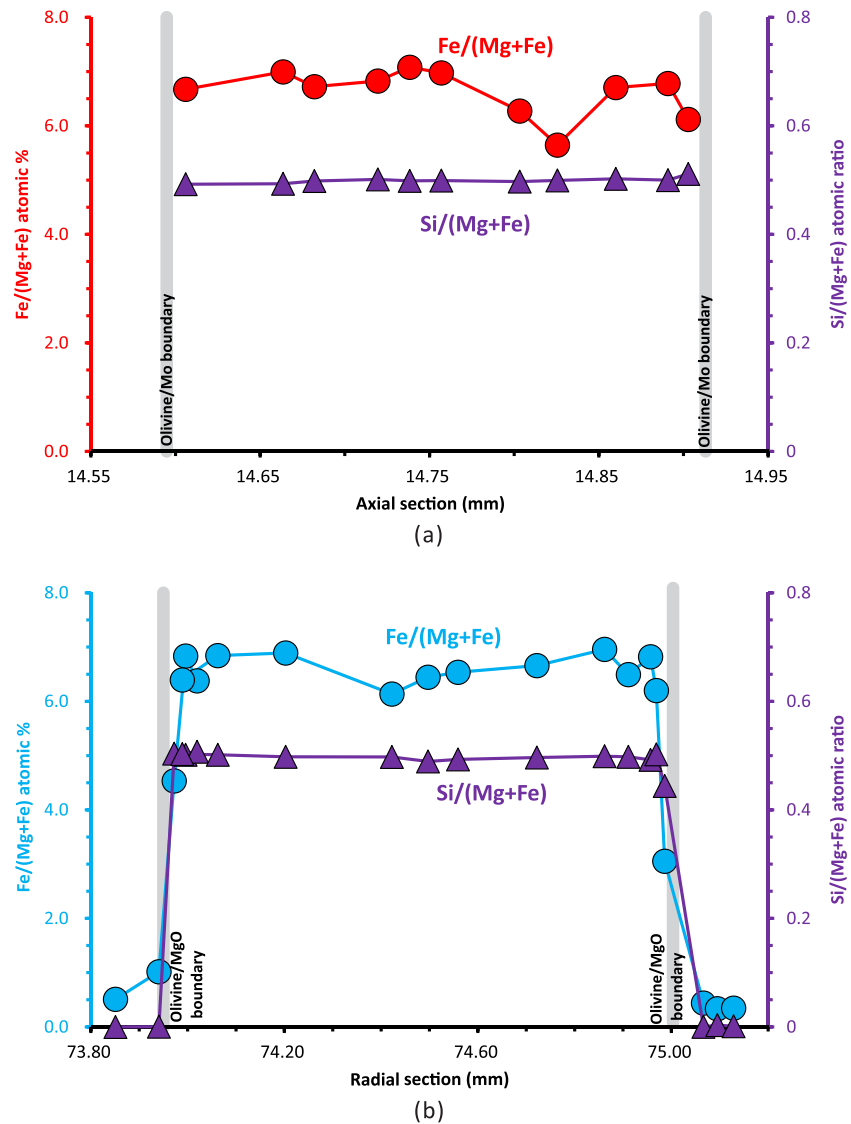


Figure 6. EPMA analysis of the recovered Sample I471. (a) Fe/(Mg + Fe) and Si/(Mg + Fe) atomic ratios across the axial section (red spots in Figure 5a). (b) Fe/(Mg + Fe) and Si/(Mg + Fe) atomic ratios across the radial section (blue spots in Figure 5b). The position data are (x, y) of the analysis points automatically recorded by the EPMA. The gray lines indicate the boundary positions of olivine/Mo and olivine/MgO. No clear reduction of Fe/(Mg + Fe) is found in the distance of ~10 μm from the Mo.

$$\sigma = \sigma_{\text{ionic}} + \sigma_{\text{sp}} = \frac{\sigma_{\text{ionic},0}}{T} \exp\left(-\frac{E_{\text{ionic}} + PV_{\text{ionic}}}{RT}\right) + \sigma_{\text{sp},0} \exp\left(-\frac{E_{\text{sp}} + PV_{\text{sp}}}{RT}\right) \quad (2)$$

where σ_0 is the preexponential factor, P is the pressure, T is the absolute temperature, R is the ideal gas constant, E is the activation energy, and V is the activation volume. Subscripted “ionic” and “sp” denote ionic and small polaron conduction mechanisms, respectively. The fitted parameters are listed in Table 1.

Both the E_{ionic} (250–405 kJ/mol) and V_{ionic} (3.2–5.3 cm^3/mol) determined in this study are substantially larger than those of proton conduction (<100 kJ/mol, <1 cm^3/mol) (Dai & Karato, 2014a, 2014b; Poe et al., 2010; Wang et al., 2006; Yang, 2012; Yoshino et al., 2006, 2009) and small polaron conduction (<160 kJ/mol, ~0 cm^3/mol) (Du Frane et al., 2005; Yoshino et al., 2009, 2012) and within experimental uncertainty identical to those of Mg (Fe) self-diffusion (~200–400 kJ/mol, 1.0–4.3 cm^3/mol) (Chakraborty et al., 1994; Fei et al., 2018a) (Tables 1 and 2). These comparisons confirm that the first term in equation 2 is Mg (Fe)

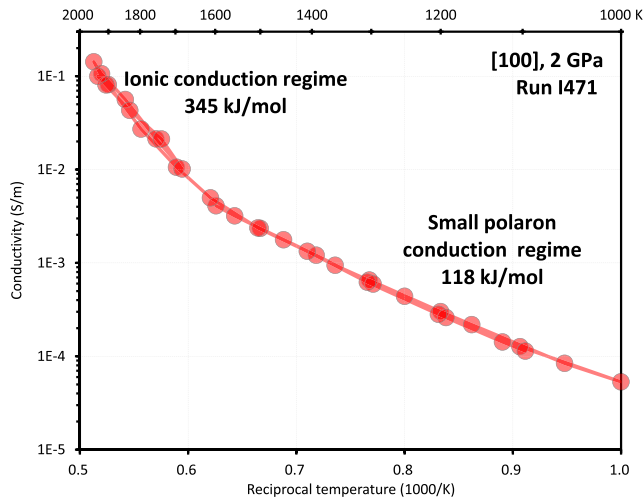


Figure 7. Two conduction mechanisms (high- and low-temperature regimes) with different temperature dependences. The high-temperature regime is assigned as ionic conduction, whereas low-temperature regime is assigned as small polaron conduction (or other mechanisms in high- C_{H_2O} runs).

self-diffusion-controlled ionic conduction. Although the apparent negative pressure dependence of conductivity may theoretically be owing to continuous dehydration under increasing pressure, this possibility is highly unlikely because both the Mg self-diffusion coefficient and ionic conductivity under dry conditions (namely, no dehydration) show strong pressure dependences (Fei et al., 2018a; Yoshino et al., 2017).

Trace amounts of brucite were used as the H_2O source in Runs H4721 and H4745; however, there should be no melts or fluid phases to affect σ_{ionic} . This is verified by the consistent E_{ionic} values obtained in brucite-bearing and brucite-free runs, that is, H4694 (no brucite, $E_{ionic} = 305(9)$ kJ/mol) and H4721 (with brucite, $E_{ionic} = 247(20)$ kJ/mol) in the [001] direction, I511 (no brucite, $E_{ionic} = 396(25)$ kJ/mol) and H4745 (with brucite, $E_{ionic} = 406(3)$ kJ/mol) in the [010] direction, and by the substantially larger activation enthalpy than those reported for fluid phase dominated conductivity (typically 30–60 kJ/mol, Gaillard et al., 2008; Sifré et al., 2014). The data obtained in H4721 and H4745 should therefore represent the conductivity of H_2O -bearing olivine rather than melt or fluid phases by excess H_2O from brucite.

The E_{ionic} along the [010] axis in the high- and low- C_{H_2O} runs (H4745 and I511) are essentially identical, whereas the data fitting indicates that E_{ionic} along [001] may be C_{H_2O} -dependent (Table 1). However, the low E_{ionic} in Runs H4721 and H4694 is likely owing to the relatively high small polaron conductivity along [001] (Constable et al., 1992), which leads to large uncertainties in the E_{ionic} determination when the experimental temperature is relatively low.

The second term in equation 2 is suggested to be small polaron conduction because E_{sp} and V_{sp} are about 120–160 kJ/mol (except for the high C_{H_2O} runs) and ~ 0 cm³/mol, respectively, both of which are comparable with previously reported values (e.g., Constable et al., 1992; Yoshino et al., 2009, 2012) (Table 2). The E_{sp}

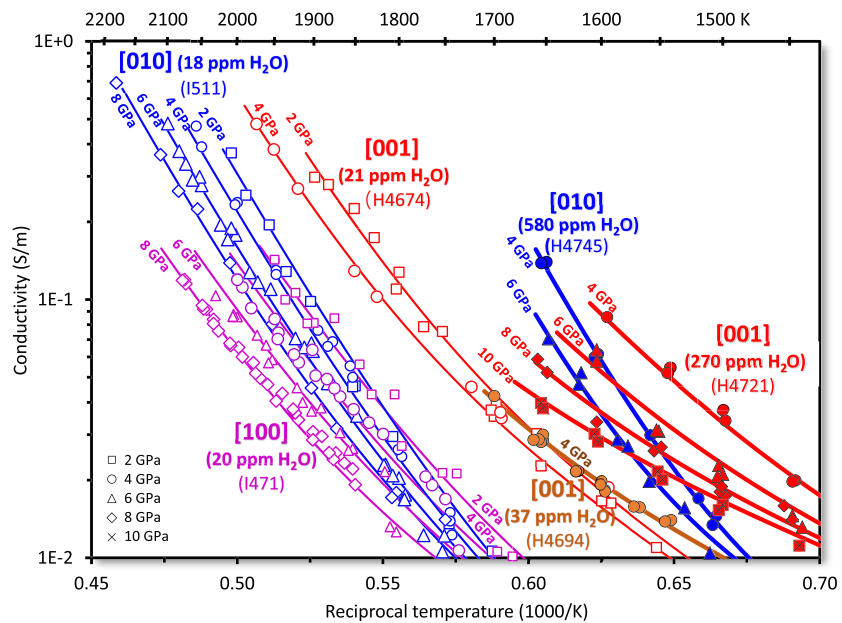


Figure 8. Olivine conductivity under various pressure, temperature, C_{H_2O} , and crystallographic orientation conditions. The bending of the fitting lines at relatively low temperatures is owing to contributions of low-temperature mechanisms. Only repeatable data points from different heating-cooling cycles are shown.

Table 2

Comparison of Activation Energy (E), Activation Volume (V), C_{H_2O} Exponent, and Anisotropy for Ionic, Small Polaron, and Proton Conductions, and Mg Self-Diffusion in Olivine

| | E (kJ/mol) | V (cm ³ /mol) | C_{H_2O} exponent | Anisotropy | References |
|--------------------------|----------------------|----------------------------|---------------------|---------------------------------|--|
| Ionic conduction | 220–405 | 3.2–5.3 | 1.3 ± 0.2^a | [001] > [100] \approx [010] | This study; Yoshino et al. (2009) |
| Mg self-diffusion | 250–400 | 1.0–4.3 | 1.2 ± 0.2 | [001] > [100] > \approx [010] | Chakraborty et al. (1994); Fei et al. (2018a) |
| Small polaron conduction | 120–160 ^b | <1 | 0 | [001] > [100] > [010] | This study; Yoshino et al. (2009, 2012) |
| Proton conduction | <100 | <1 | 0.6–1.0 | Inconsistent with each other | Dai and Karato (2014a, 2014b); Poe et al. (2010); Wang et al. (2006); Yang (2012); Yoshino et al. (2006; 2009) |

^a 1.3 ± 0.2 is obtained by data fitting of [010] and [001] runs at 1700 K and assumed to be the same for [100]. ^b(Activation energy for the low-temperature conduction regime of Runs H4745, H4721, and H4694 is <115 kJ/mol (Table 1). This might be caused by the contribution of other mechanisms and is therefore not assigned as small polaron conduction here).

obtained in Runs H4721, H4745, and H4694 are considerably lower (<115 kJ/mol) than others (Table 1). This might be because the temperature ranges for these runs were substantially smaller than others and the E_{sp} determination therefore became less precise or because the small polaron mechanism is masked by other mechanisms (e.g., proton mechanism if it is valid).

Ionic conduction is found to be significantly anisotropic. The σ_{ionic} along the [001] axis ($\sigma_{ionic[001]}$) is 3–5 times higher than that along the [100] and [010] axes ($\sigma_{ionic[100]}$ and $\sigma_{ionic[010]}$, respectively), that is, $\sigma_{ionic[001]} \gg \sigma_{ionic[100]} \approx \sigma_{ionic[010]}$ (Figure 8). This order is identical to that of Mg self-diffusivity ($D_{[001]} \approx 4D_{[100]} \approx 6D_{[010]}$, Chakraborty et al., 1994), as well as to that of ionic conductivity at ambient pressure (Constable et al., 1992). Mg defects are primarily located on sites with $\tilde{\Gamma}$ symmetry (M1), and the migration distances of M1 defects are in the order of [001] \ll [100] $<$ \approx [010] (longer distance means more difficult for migration, Ottonello et al., 1990; Brodholt, 1997). The anisotropy of both ionic conduction and self-diffusion can therefore be explained by the anisotropic hopping distances of defects on M1 sites (Brodholt, 1997; Constable et al., 1992).

Most importantly, olivine with \sim 270–580 wt. ppm H₂O has more than 1 order of magnitude higher conductivity than those with \sim 20 wt. ppm H₂O (Figure 8). On the basis of the simulation of the fitting parameters for the σ_{ionic} term in Table 1, both $\sigma_{ionic[010]}$ and $\sigma_{ionic[001]}$ at 1700 K (average asthenospheric temperature beneath young plates, that is, about 1600 and 1800 K at 100 and 410 km depth, respectively, for a 5 My geotherm, Katsura et al., 2017; Turcotte & Schubert, 2002) show

$$\sigma_{ionic[hkl]} \propto (C_{H_2O})^{1.3 \pm 0.2} \quad (3)$$

Note that the absolute bulk conductivity values obtained in different runs cannot be directly compared owing to the various contributions of the low-temperature mechanisms.

Because σ_{ionic} has different temperature dependences in different runs, the C_{H_2O} exponent varies slightly with temperature during data fitting, but remain within uncertainty under the asthenospheric temperature range (i.e., \sim 1.5 at 1500 K and \sim 1.2 at 1800 K). In any case, the C_{H_2O} exponent remains in the range of 1.0–1.7 even though the C_{H_2O} based on unpolarized FTIR analysis may have uncertainties as large as a factor of 2. The large C_{H_2O} dependence of ionic conductivity has therefore been demonstrated by direct measurement following our previous prediction based on Mg self-diffusivity, which has a C_{H_2O} exponent of 1.2 ± 0.2 (Fei et al., 2018a). This large C_{H_2O} exponent is expected because defect migration on Mg (Fe) sites in hydrous olivine occurs by the exchange of species among V_{Me}'' , $(2H)_{Me}^{\times}$, and Me_{Me}^{\times} , and the concentration of $(2H)_{Me}^{\times}$ is proportional to C_{H_2O} according to the hydration process of Mg sites, $Mg_{Mg}^{\times} + H_2O \rightarrow (2H)_{Mg}^{\times} + MgO$ (Kohlstedt, 2006; Kohlstedt & Mackwell, 1998). A C_{H_2O} exponent larger than 1.0 also suggests that defect concentration and mobility are both enhanced by hydration (Fei et al., 2018a).

The H₂O dependence of $\sigma_{ionic[100]}$ is not determined in this study because it is masked by small polaron conduction at relatively low temperatures (<1700 K), whereas significant dehydration occurs at >1700 K. We assume that $\sigma_{ionic[100]}$ has the same C_{H_2O} dependence as other crystallographic orientations.

Table 3

Fitting Parameters of Hydrous Olivine Conductivity Expressed as in Equations 4–9, Where C_{H_2O} Is the H_2O Content in wt. ppm Based on Withers et al. (2012)

| Axis | r | $\text{Log}\sigma_{\text{ionic},0}[\text{hkl}]$ (K·S/m) | $E_{\text{ionic}[\text{hkl}]}$ (kJ/mol) | $V_{\text{ionic}[\text{hkl}]}$ (cm^3/mol) | $\text{Log}\sigma_{\text{sp},0}[\text{hkl}]$ (S/m) | $E_{\text{sp}[\text{hkl}]}$ (kJ/mol) | $V_{\text{sp}[\text{hkl}]}$ (cm^3/mol) | Misfit |
|-----------|------------------------|--|--|--|---|---|---|--------|
| [100] | 1.3 (0.2) ^a | 9.9 (5) | 337 (15) | 4.2 (4) | 1.5 (2) | 117 (13) | 0.5 (7) | 0.04 |
| [010] | | 11.6 (4) | 396 (25) | 3.2 (2) | 2.7 (2) | 163 (25) | −0.2 (2) | 0.06 |
| [001] | | 11.8 (4) | 385 (15) | 4.1 (4) | 2.7 (3) | 139 (13) | 0.5 (7) | 0.15 |
| Isotropic | | 11.1 | 372 | 3.8 | 2.3 | 139 | 0.3 | — |

^aThe H_2O content exponent, r , is assumed to be the same for different orientations.

Theoretically, we cannot exclude the possibility of anisotropic C_{H_2O} dependence, but it is a reasonable assumption because H substitution is independent of orientation, whereas the weakening of Mg^{2+} bonding by hydration along different directions is expected to be similar because the overall bond strength of Mg^{2+} is weakened.

3.4. Ionic Conductivity of Olivine Under Asthenospheric Conditions

Using the pressure, temperature, C_{H_2O} , and crystallographic dependences determined in this study, the integrated models of anisotropic conductivity along [hkl] axis ($\sigma_{\text{ionic}[\text{hkl}]}$ and $\sigma_{\text{sp}[\text{hkl}]}$ for ionic and small polaron conductivities, respectively) and isotropic conductivity ($\sigma_{\text{ionic}[\text{iso}]}$ and $\sigma_{\text{sp}[\text{iso}]}$, respectively) in hydrous olivine under asthenospheric conditions are given as

$$\sigma_{\text{ionic}[\text{hkl}]} = \sigma_{\text{ionic}[\text{hkl}]}^{(\text{anhydrous})} + \sigma_{\text{ionic}[\text{hkl}]}^{(\text{hydrous})} \approx \frac{\sigma_{\text{ionic},0}[\text{hkl}]}{T} (C_{H_2O})^r \exp\left(-\frac{E_{\text{ionic}[\text{hkl}]} + PV_{\text{ionic}[\text{hkl}]}}{RT}\right) \quad (4)$$

$$\sigma_{\text{ionic}[\text{iso}]} = (\sigma_{\text{ionic}[\text{100}]} \times \sigma_{\text{ionic}[\text{010}]} \times \sigma_{\text{ionic}[\text{001}]})^{1/3} \quad (5)$$

$$\sigma_{\text{sp}[\text{hkl}]} = \sigma_{\text{sp},0}[\text{hkl}] \exp\left(-\frac{E_{\text{sp}[\text{hkl}]} + PV_{\text{sp}[\text{hkl}]}}{RT}\right) \quad (6)$$

$$\sigma_{\text{sp}[\text{iso}]} = (\sigma_{\text{sp}[\text{100}]} \times \sigma_{\text{sp}[\text{010}]} \times \sigma_{\text{sp}[\text{001}]})^{1/3} \quad (7)$$

The bulk conductivity of anisotropic and isotropic models are

$$\sigma_{\text{bulk}[\text{hkl}]} = \sigma_{\text{ionic}[\text{hkl}]} + \sigma_{\text{sp}[\text{hkl}]} \quad (8)$$

$$\sigma_{\text{bulk}[\text{iso}]} = \sigma_{\text{ionic}[\text{iso}]} + \sigma_{\text{sp}[\text{iso}]} \quad (9)$$

The fitting parameters of $\sigma_{\text{ionic},0}$, E_{ionic} , V_{ionic} , $\sigma_{\text{sp},0}$, E_{sp} , and V_{sp} are listed in Table 3. The C_{H_2O} is in wt. ppm based on Withers et al. (2012), $\sigma_{\text{ionic}[\text{hkl}]}^{(\text{anhydrous})}$ is ionic conductivity in dry olivine, and $\sigma_{\text{ionic}[\text{hkl}]}^{(\text{hydrous})}$ is ionic conductivity owing to H_2O incorporation. Because $\sigma_{\text{ionic}[\text{hkl}]}^{(\text{anhydrous})}$ based on completely dry experiments at ambient pressure (Constable et al., 1992) is more than 1 order of magnitude lower than our experimental data with ~20 wt. ppm H_2O (Figure 8), the contribution of $\sigma_{\text{ionic}[\text{hkl}]}^{(\text{anhydrous})}$ is considered negligible in this study, as expressed in equation 4. The transition of ionic conduction from an anhydrous to hydrous mechanism should occur at C_{H_2O} much lower than 20 wt. ppm. The r is assumed to be 1.3 ± 0.2 for different crystallographic orientations and independent of temperature and pressure, whereas E_{ionic} and V_{ionic} are assumed to be independent from C_{H_2O} (Table 3). These assumptions are expected to have little effect on the simulated results because our conductivity data were obtained under asthenospheric P - T conditions, and the range of C_{H_2O} extrapolation is small owing to the relatively low (30–60 wt. ppm) H_2O content of olivine in the depleted MORB mantle (Demouchy & Bolfan-Casanova, 2016; Katsura et al., 2017).

The simulated results of σ_{ionic} for isotropic and anisotropic models under the topmost asthenospheric conditions (3 GPa) are plotted in Figures 9a and 9b, whereas the bulk conductivity, which is the summation of different mechanisms, are plotted in Figure 9c. The σ_{ionic} in this study shows a comparable

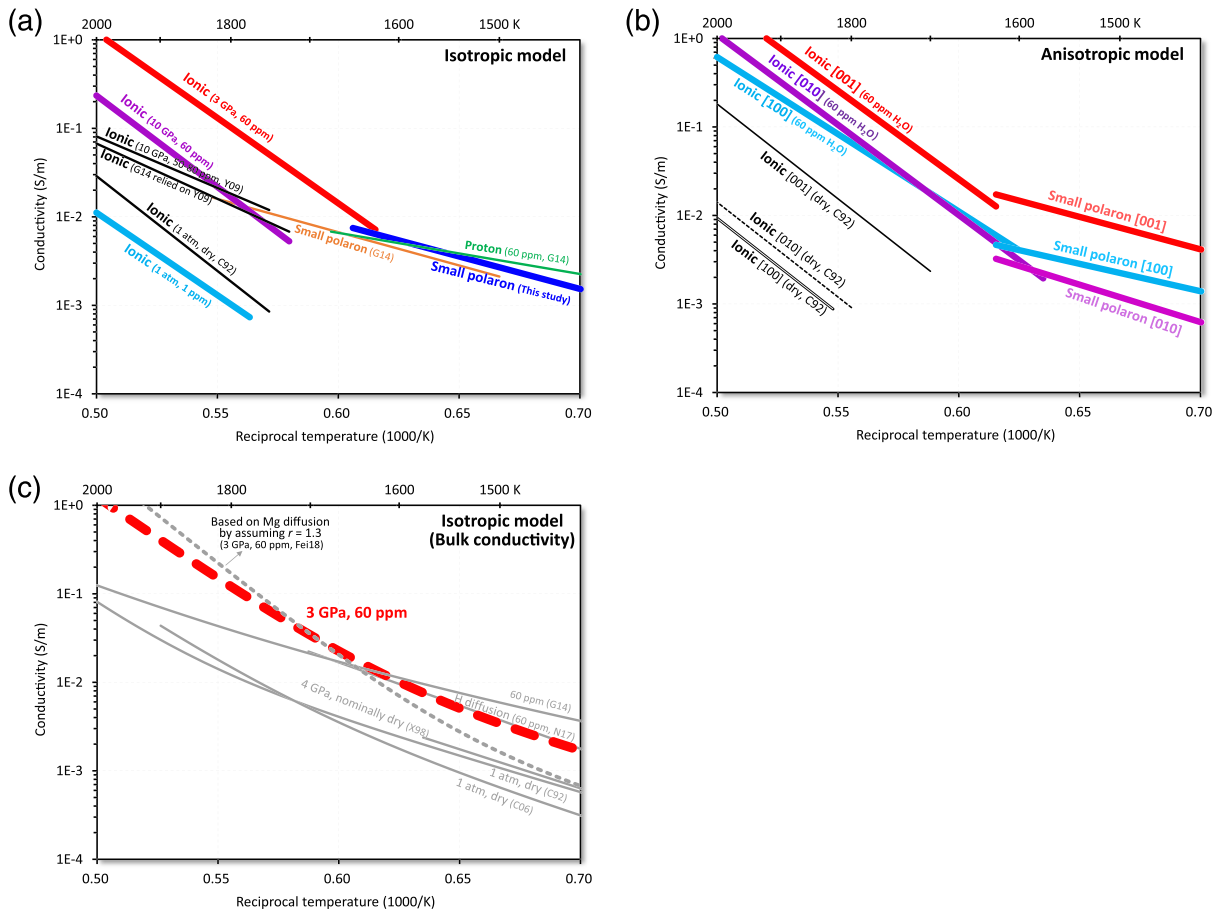


Figure 9. Ionic conductivity in olivine with 60 wt. ppm H_2O is higher than dry olivine conductivity and higher than small polaron and proton conductivities as well. The thick lines are simulations from this study based on equations 4–9 with all parameters given in Table 3. (a) Isotropic model with separation of different conduction mechanisms. (b) Anisotropic model with separation of different conduction mechanisms. (c) Isotropic model of bulk conductivity. N17: Novella et al. (2017) based on hydrogen diffusion experiments. Y09: Yoshino et al. (2009). C92: Constable et al. (1992). G14: Gardés et al. (2014). C06: Constable (2006). X98: Xu et al. (1998). Fe18: Fei et al. (2018a). Fei et al. (2018a) is based on conductivity data reported by Constable et al. (1992) with pressure and C_{H_2O} corrections using the activation energy and C_{H_2O} exponent for Mg diffusivity by assuming proportionality of $C_{H_2O}^{1.3}$ and σ_{ionic} at $C_{H_2O} \geq 1$ wt. ppm. Although a correction factor of 3 in equation 1 was not applied in Fei et al. (2018a), the absolute values of C_{H_2O} were not used for the simulation and therefore do not affect the σ_{ionic} estimation.

temperature dependence with the previously reported ionic conductivity data (e.g., Constable et al., 1992), indicating the same conduction mechanisms (Figures 9a and 9b). After adjusting to a C_{H_2O} of 1 wt. ppm, the isotropic σ_{ionic} from this study is comparable with σ_{ionic} reported in dry olivine at ambient pressure (Constable et al., 1992). However, by adding 60 wt. ppm H_2O (the maximum C_{H_2O} for olivine in the depleted mantle by considering H_2O partitioning in upper mantle minerals, Demouchy & Bolfan-Casanova, 2016), σ_{ionic} is enhanced by about 2 orders of magnitude (Figure 9a). We have $\sigma_{ionic[001]} \gg \sigma_{ionic[100]} \approx \sigma_{ionic[010]}$ in olivine with 60 wt. ppm H_2O , which has the same order of anisotropy and comparable temperature dependence as that under dry conditions at ambient pressure (Constable et al., 1992) although the absolute values differ by more than 1 order of magnitude due to the H_2O enhancement.

The isotropic σ_{ionic} from our model at 10 GPa is within experimental uncertainty consistent with that reported by Yoshino et al. (2009) under similar conditions due to the negative pressure dependence (Figure 9a). The 3 GPa data are comparable with that estimated from hydrogen diffusivity as well by assuming a linear relationship between C_{H_2O} and hydrogen-related σ (Du Frane & Tyburczy, 2012; Novella et al., 2017), which is not surprising because hydrogen diffusion is the migration of protons into/out of cation sites and is therefore also controlled by Mg defects.

Owing to the H₂O-enhancement of σ_{ionic} , the bulk conductivity obtained in this study with 60 wt. ppm H₂O is clearly higher than values reported under dry conditions (Constable, 2006; Constable et al., 1992; Xu et al., 1998) and comparable with that estimated from Mg diffusion by assuming an $C_{\text{H}_2\text{O}}$ exponent of 1.3 (Fei et al., 2018a) (Figure 9c). However, although the absolute values of our bulk conductivity data are identical to Gardés et al.'s (2014) model at 1600–1700 K, the temperature dependences are completely different, indicating the dominance of different mechanisms. This inconsistency is likely caused by an overestimation of proton conductivity in previous studies (see discussion in the supporting information).

The comparison of σ_{ionic} and σ_{sp} (and proton conduction) shows a mechanism transition from small polaron to ionic conduction at 1600–1650 K (Figures 9a and 9b). This transition temperature, although pressure- and $C_{\text{H}_2\text{O}}$ -dependent, is much lower than the previously estimated values (>1750 K, Gardés et al., 2014; Yoshino et al., 2009) and comparable with the asthenospheric geotherm (Katsura et al., 2017; Turcotte & Schubert, 2002). Therefore, by H₂O-enhancement, σ_{ionic} of olivine is nonnegligible under asthenospheric conditions. It may contribute significantly, or dominate the bulk conductivity of olivine in the asthenosphere especially in the shallow region beneath young plates where the pressure is relatively low and temperature is relatively high.

Based on our model, the bulk conductivity of olivine with 60 wt. ppm H₂O is $>10^{-2}$ S/m when the temperature is above 1600 K (Figure 9c), which is comparable with the high conductivity observed at the topmost asthenosphere beneath young plates (Baba et al., 2006). On the other hand, the asthenosphere is associated with low seismic velocity, which cannot be attributed to olivine hydrated with only tens of wt. ppm H₂O (Cline et al., 2018). By considering the fact that the high conductivity is observed mostly beneath young plates (summarized in Katsura et al., 2017) whereas the low seismic velocity zone is detected nearly globally, the origins of these geophysical features could be different, although they occur at similar depths.

Acknowledgments

We thank S. Linhardt for technical assistance of in situ impedance analysis, R. Njul for sample preparation, H. Fisher for machining high-pressure cell assemblies, and A.C. Withers for helpful discussion. Comments from W. L. Du Frane and anonymous reviewers are helpful to improve the manuscript. This work is financially supported by the German Research Foundation (DFG) to T. Katsura (KA3434/3-1, KA3434/3-2, KA3434/7-1, KA3434/8-1, and KA3434/9-1). The data for this paper are given in Tables 11–3 and in the general repository, Zenodo (doi: 10.5281/zenodo.3386773).

References

- Baba, K., Chave, A. D., Evans, R. L., Hirth, G., & Mackie, R. L. (2006). Mantle dynamics beneath the East Pacific rise at 17°S: Insights from the mantle electromagnetic and tomography (MELT) experiment. *Journal of Geophysical Research*, *111*, B02101. <https://doi.org/10.1029/2004JB003598>
- Bell, D. R., Rossman, G. R., Maldener, J., Endisch, D., & Rauch, F. (2003). Hydroxide in olivine: A quantitative determination of the absolute amount and calibration of the IR spectrum. *Journal of Geophysical Research*, *108*(B2), 2105. <https://doi.org/10.1029/2001JB000679>
- Brodholt, J. (1997). Ab initio calculations on point defects in forsterite (Mg₂SiO₄) and implications for diffusion and creep. *American Mineralogist*, *82*, 1049–1053.
- Chakraborty, S., Farver, J. R., Yund, R. A., & Rubie, D. C. (1994). Mg trace diffusion in synthetic forsterite and San Carlos olivine as a function of P, T, and f_{O_2} . *Physics and Chemistry of Minerals*, *21*, 489–500.
- Cline, C. J. II, Faul, U. H., David, E. C., Berry, A. J., & Jackson, I. (2018). Redox-influenced seismic properties of upper-mantle olivine. *Nature*, *555*, 355–358.
- Constable, S. (2006). SEO3: A new model of olivine electrical conductivity. *Geophysical Journal International*, *166*, 435–437.
- Constable, S., Shankland, T. J., & Duba, A. G. (1992). The electrical conductivity of an isotropic olivine mantle. *Journal of Geophysical Research*, *83*, 3397–3404.
- Dai, L., & Karato, S. I. (2014a). High and highly anisotropic electrical conductivity of the asthenosphere due to hydrogen diffusion in olivine. *Earth and Planetary Science Letters*, *408*, 79–86.
- Dai, L., & Karato, S. I. (2014b). The effect of pressure on the electrical conductivity of olivine under the hydrogen-rich conditions. *Physics of the Earth and Planetary Interiors*, *232*, 51–56.
- Demouchy, S., & Bolfan-Casanova, N. (2016). Distribution and transport of hydrogen in the lithospheric mantle: A review. *Lithos*, *240*, 402–425.
- Demouchy, S., & Mackwell, S. (2006). Mechanisms of hydrogen incorporation and diffusion in iron-bearing olivine. *Physics and Chemistry of Minerals*, *33*, 347–355.
- Du Frane, W. L., Roberts, J. J., Toffelmier, D. A., & Tyburczy, J. A. (2005). Anisotropy of electrical conductivity in dry olivine. *Geophysical Research Letters*, *32*, L24315. <https://doi.org/10.1029/2005GL023879>
- Du Frane, W. L., & Tyburczy, J. A. (2012). Deuterium-hydrogen exchange in olivine: Implications for point defects and electrical conductivity. *Geochemistry, Geophysics, Geosystems*, *13*, Q03004. <https://doi.org/10.1029/2011GC003895>
- Evans, R. L., Hirth, G., Baba, K., Forsyth, D., Chave, A., & Mackie, R. (2005). Geophysical evidence from the MELT area for compositional controls on oceanic plates. *Nature*, *437*(7056), 249–252. <https://doi.org/10.1038/nature04014>
- Fei, H., Huang, R., & Yang, X. (2017). CaSiO₃-perovskite may cause electrical conductivity jump in the topmost lower mantle. *Geophysical Research Letters*, *44*, 10,226–10,232. <https://doi.org/10.1002/2017GL075070>
- Fei, H., Koizumi, S., Sakamoto, N., Hashiguchi, M., Yurimoto, H., Marquardt, K., et al. (2018a). Mg lattice diffusion in iron-free olivine and implications to conductivity anomaly in the oceanic asthenosphere. *Earth and Planetary Science Letters*, *484*, 204–212.
- Fei, H., Koizumi, S., Sakamoto, N., Hashiguchi, M., Yurimoto, H., Marquardt, K., et al. (2018b). Pressure, temperature, water content, and oxygen fugacity dependence of the Mg grain-boundary diffusion coefficient in forsterite. *American Mineralogist*, *103*, 1354–1361.
- Fei, H., Wiedenbeck, M., Yamazaki, D., & Katsura, T. (2013). Small effect of water on upper-mantle rheology based on Silicon self-diffusion coefficients. *Nature*, *498*, 213–215.

- Fei, H., Wiedenbeck, M., Yamazaki, D., & Katsura, T. (2014). No effect of water on oxygen self-diffusion rate in forsterite. *Journal of Geophysical Research: Solid Earth*, 119, 7598–7606.
- Gaillard, F., Malki, M., Iacono-Marziano, G., Pichavant, M., & Scaillet, B. (2008). Carbonatite melts and electrical conductivity in the asthenosphere. *Science*, 322(5906), 1363–1365. <https://doi.org/10.1126/science.1164446>
- Gardés, E., Gaillard, F., & Tarits, P. (2014). Toward a unified hydrous olivine electrical conductivity law. *Geochemistry, Geophysics, Geosystems*, 15, 4984–5000. <https://doi.org/10.1002/2014GC005496>
- Gardés, E., Gaillard, F., & Tarits, P. (2015). Comments to “High and highly anisotropic electrical conductivity of the asthenosphere due to hydrogen diffusion in olivine” by Dai and Karato [Earth Planet. Sci. Lett. 408 (2014) 79–96]. *Earth and Planetary Science Letters*, 427, 296–299.
- Gose, J., Schmadicke, E., Markowitz, M., & Beran, A. (2010). OH point defects in olivine from Pakistan. *Mineralogy and Petrology*, 99, 105–111.
- Karato, S. (2019). Some remarks on hydrogen-assisted electrical conductivity in olivine and other minerals. *Progress in Earth and Planetary Science*, 6(1), 1–19. <https://doi.org/10.1186/s40645-019-0301-2>
- Katsura, T., Baba, K., Yoshino, T., & Kogiso, T. (2017). Electrical conductivity of the oceanic asthenosphere and its interpretation based on laboratory measurements. *Tectonophysics*, 717, 162–171.
- Kohlstedt, D. L. (2006). The role of water in high-temperature deformation. *Reviews in Mineralogy and Geochemistry*, 62, 377–396.
- Kohlstedt, D. L., & Mackwell, S. (1998). Diffusion of hydrogen and intrinsic point defects in olivine. *Zeitschrift für Physikalische Chemie*, 207, 14–162.
- Novella, D., Jacobsen, B., Weber, P. K., Tyburczy, J. A., Ryerson, F. J., & Du Frane, W. L. (2017). Hydrogen self-diffusion in single crystal olivine and electrical conductivity of the Earth’s mantle. *Scientific Reports*, 7(1), 5344. <https://doi.org/10.1038/s41598-017-05113-6>
- Otonello, G., Princivalle, F., & Giusta, A. D. (1990). Temperature, composition, and f_{O_2} effects on intersite distribution of Mg and Fe^{2+} in olivines. *Physics and Chemistry of Minerals*, 17, 301–312.
- Poe, B. T., Romano, C., Nestola, F., & Smyth, J. R. (2010). Electrical conductivity anisotropy of dry and hydrous olivine at 8 GPa. *Physics of the Earth and Planetary Interiors*, 181, 103–111.
- Sifré, D., Gardés, E., Massuyeau, M., Hashim, L., Hier-Majumder, S., & Gaillard, F. (2014). Electrical conductivity during incipient melting in the oceanic low-velocity zone. *Nature*, 509, 81–85.
- Stocker, R. L., & Smyth, D. M. (1978). Effect of enstatite activity and oxygen partial pressure on the point-defect chemistry of olivine. *Physics of the Earth and Planetary Interiors*, 16, 145–156.
- Turcotte, D. L., & Schubert, G. (2002). *Geodynamics*. Chpt., (Vol. 4, pp. 237–353). Cambridge: Cambridge University Press.
- Wang, D. J., Mookherjee, M., Xu, Y. S., & Karato, S. I. (2006). The effect of water on the electrical conductivity of olivine. *Nature*, 443(7114), 977–980. <https://doi.org/10.1038/nature05256>
- Withers, A. C. (2013). On the use of unpolarized infrared spectroscopy for quantitative analysis of absorbing species in birefringent crystals. *American Mineralogist*, 98, 689–697.
- Withers, A. C., Bureau, H., Raepsaet, C., & Hirschmann, M. M. (2012). Calibration of infrared spectroscopy by elastic recoil detection analysis of H in synthetic olivine. *Chemical Geology*, 334, 92–98.
- Xu, Y., Poe, B. T., Shankland, T. J., & Rubie, D. C. (1998). Electrical conductivity of olivine, wadsleyite, and ringwoodite under upper-mantle conditions. *Science*, 280(5368), 1415–1418. <https://doi.org/10.1126/science.280.5368.1415>
- Yang, X. (2012). Orientation-related electrical conductivity of hydrous olivine, clinopyroxene and plagioclase and implications for the structure of the lower continental crust and uppermost mantle. *Earth and Planetary Science Letters*, 317, 241–250.
- Yoshino, T., Matsuzaki, T., Shatskiy, A., & Katsura, T. (2009). The effect of water on the electrical conductivity of olivine aggregates and its implications for the electrical structure of the upper mantle. *Earth and Planetary Science Letters*, 288, 291–300.
- Yoshino, T., Matsuzaki, T., Yamashita, S., & Katsura, T. (2006). Hydrous olivine unable to account for conductivity anomaly at the top of the asthenosphere. *Nature*, 443(7114), 973–976. <https://doi.org/10.1038/nature05223>
- Yoshino, T., Shimojuku, A., Shan, S., Guo, X., Yamazaki, D., Ito, E., et al. (2012). Effect of temperature, pressure and iron content on the electrical conductivity of olivine and its high-pressure polymorphs. *Journal of Geophysical Research*, 117, B08205. <https://doi.org/10.1029/2011JB008774>
- Yoshino, T., Zhang, B., Rhymer, B., Zhao, C. C., & Fei, H. (2017). Pressure dependence of electrical conductivity in forsterite. *Journal of Geophysical Research: Solid Earth*, 122, 158–171. <https://doi.org/10.1002/2016JB013555>